THE ASTROPHYSICAL JOURNAL, 555:532–539, 2001 July 1

RESONANCE-LINE SCATTERING IN SUPERNOVA REMNANT SHOCKS

RAVI SANKRIT[1] AND KENNETH WOOD[2]
Received 2000 December 8; accepted 2001 February 28

ABSTRACT

We present a three-dimensional radiative transfer model to examine the effects of resonance-line scattering in the postshock flow behind a nonradiative supernova remnant shock. For a rippled shock front viewed edge-on, line scattering significantly reduces the observed flux of C IV λ1549 and N V λ1240, two important diagnostic lines in the ultraviolet spectra of supernova remnants. The correction factor (defined to be the ratio of the line flux that would be observed neglecting scattering to the actual observed line flux) is a function of position within the filament. For sufficiently large regions that include crisp edges as well as more diffuse regions of the filament structure, the C IV and N V correction factors are between about 1.5 and 3.5 (and the C IV correction factor is invariably larger than the N V correction factor). The correction factors have a larger range when smaller regions are considered. The C IV correction factor is about 6 at the filament edges, while the N V correction factor is about 4. These simulations of resonance-line scattering will be useful for the analysis of supernova remnant shock spectra.

Subject headings: radiative transfer — shock waves — supernova remnants — ultraviolet: ISM

1. INTRODUCTION

The optical and ultraviolet emission from middle-aged supernova remnants (SNRs) arises mainly in shock-excited gas. The shocks are driven by the supernova blast wave into surrounding interstellar clouds. Several lines from a range of ionization states are seen in the spectra of these shocks. The line strengths can be used to obtain properties such as the shock velocity, the preshock density, and the elemental abundances (e.g., Raymond 1991).

A standard method of interpreting SNR spectra is to compare observed line fluxes with shock model predictions and thereby derive the shock properties. Raymond et al. (1980) pointed out that radiative transfer in resonance lines (permitted lines to the ground state) was a potential problem in comparing observations with model calculations. Their models showed that the optical depths of resonance lines are of order unity in the flow direction, and much higher along the line of sight when the shock is viewed edge-on. They found that models which correctly predicted the observed intensities of intercombination lines in an *International Ultraviolet Explorer* spectrum of a filament in the Cygnus Loop SNR severely underpredicted the observed resonance-line intensities. They ascribed this discrepancy to resonance-line scattering in the filament. The same discrepancy between observed and predicted strengths of resonance lines relative to nonresonance lines was found in other studies of SNR shocks as well (Raymond et al. 1981, 1988, 1997). Resonance-line scattering effects were directly observed by Cornett et al. (1992). In images of a large field in the Cygnus Loop taken with the Ultraviolet Imaging Telescope, they found that the C IV λ1549 emission was significantly reduced near sharp optical filaments, which are the locations where the shock is viewed close to edge-on (Hester 1987).

Thus, it has been known for some time that the observed fluxes of resonance lines have to be corrected for optical depth effects when analyzing SNR shock spectra. The approach toward this problem has been, for the most part, to obtain shock velocities and preshock densities based on nonresonance lines and then to calculate the effects of resonance-line scattering by comparing the observed fluxes with the fluxes predicted by a "best fit" model. That is, the resonance-line strengths themselves were not used in the analysis. In one study of filaments in Vela and in the Cygnus Loop, Raymond et al. (1981) calculated line optical depths from column densities predicted by shock models. Having assumed a thin sheet geometry viewed edge-on and single scattering, they found attenuation factors for several resonance lines. As they point out, these values are extreme because of the assumed geometry. Raymond et al. (1981) further state that quantitative interpretation of the resonance-line strengths is extremely difficult because the line strengths depend on details of the geometry and on the shock properties.

Resonance-line scattering also affects the ratio between the line strengths of the components of a resonance doublet such as O VI $\lambda\lambda$1032, 1038. If the emission is optically thin, then the observed ratio, I_{1038}/I_{1032}, should be 0.5. For higher optical depth, the ratio will increase and, in the optically thick case, be equal to 1.0. The O VI doublet was partly resolved in a Hopkins Ultraviolet Telescope (HUT) spectrum of a nonradiative filament in the Cygnus Loop (Long et al. 1992). The observed ratio I_{1038}/I_{1032} was 0.6, indicating an optical depth of about 1 for the 1032 Å line, and a reduction of the total O VI flux by a factor of 1.4. The use of this method depends on having sufficient spectral resolution to resolve the doublet components. Furthermore, it has long been known from numerical models that the emission from SNR shocks is highly stratified. The O VI emission does not trace lower ionization species such as N V and C IV. Therefore, the O VI $\lambda\lambda$1032, 1038 optical depth cannot be used to derive the optical depths of lines such as N V λ1240 and C IV λ1549.

In this paper, we introduce a method using a Monte Carlo transfer code to calculate the effect of resonance-line scattering in SNR shocks. The effort has been motivated in part by the spatially resolved ultraviolet spectra of SNRs

[1] Department of Physics and Astronomy, Johns Hopkins University, 3400 North Charles Street, Baltimore, MD 21218.
[2] Harvard-Smithsonian Center for Astrophysics, 60 Garden Street, Cambridge, MA 02138.

that can be obtained by new instruments such as the Space Telescope Imaging Spectrograph (STIS) on board the *Hubble Space Telescope* and the *Far Ultraviolet Spectroscopic Explorer*. An example of such spectra are those of a nonradiative shock in the Cygnus Loop obtained with STIS. (This is the same filament observed by Long et al. 1992, referred to above.) One spectrum, taken with the spatial axis of the spectrograph slit placed perpendicular to the shock front, shows the ionization stratification of the postshock gas (Sankrit et al. 2000, hereafter SBRL). The other spectra have been taken with the slit placed parallel to the shock front at different positions, providing a map of the C IV and N V emission in the postshock flow. These two lines are the only strong lines seen in the STIS spectra. In order to interpret the data, it is necessary to treat resonance-line scattering more accurately than has so far been done.

We base the shock model on a well-studied nonradiative shock in the northeast region of the Cygnus Loop. The shock is assumed to have a rippled, thin sheet geometry, as seen in a Wide Field Planetary Camera 2 (WFPC2) Hα image (Blair et al. 1999). The properties of the gas in the postshock flow are specified using shock model predictions (SBRL). The shock model is calculated in one dimension and applied at every point on the rippled surface to generate the three-dimensional density distribution. In § 2 we describe the Monte Carlo code and the details of the model filament. The results from the scattering calculations are presented in § 3. Finally, in § 4 we discuss the implications of our work and suggest ways in which the method can be used in future studies of SNR shocks.

2. MODEL DESCRIPTION

The Monte Carlo code we use for our simulations is based on the one described by Code & Whitney (1995) and has been modified to run on a three-dimensional Cartesian grid (Wood & Reynolds 1999). The code tracks energy packets as they are scattered within a density grid. For a total luminosity L of the grid, N energy packets are tracked over a time interval Δt, so each packet has an energy $E_\gamma = L\Delta t/N$. Hereafter, we refer to an energy packet as a "photon." The emissivity of a given line and the number density of the species that emits the line are provided as functions of position. The code calculates the surface brightness as seen from a specified viewing direction. The code does not treat radiative transfer within the line; instead, it considers all photons to be emitted and resonantly scattered at a single wavelength. This approximation is valid for moderate optical depths where photons are not scattered out of the Doppler core of the line. The code includes forced first scattering (Witt 1977) and a "peeling off" procedure (Yusef-Zadeh, Morris, & White 1984), which allow us to construct model images of three-dimensional structures from any specified viewing angle very efficiently.

We use the nonradiative shock in the northeast limb of the Cygnus Loop studied most recently by Blair et al. (1999) and SBRL as the physical basis for our model. The Hα emission from a nonradiative shock is due to collisional excitation of neutrals in a narrow zone ($\sim 2 \times 10^{14}$ cm) behind the shock front. Therefore, the WFPC2 Hα image presented by Blair et al. (1999) shows us the morphology of the shock front. The essential morphological features of the shock front can be captured by modeling the rippled sheet geometry with a simple superposition of sine waves. We obtained the equation for the shock-front geometry by trial and error, visually comparing with the WFPC2 Hα image. With lengths in code units ($R_0 = 10^{15}$ cm), the equation used is

$$z = 3.5\left[2 \sin \frac{2\pi(x - 200)}{1000} + \sin \frac{2\pi x}{500}\right] \times \left(2 \sin \frac{2\pi y}{1000} + \sin \frac{2\pi y}{500}\right). \quad (1)$$

Thus, the shock front lies approximately in the x-y plane. The physical dimensions of the grid used for the calculations are 6×10^{17} cm along each of the x- and y-axes and 6×10^{16} cm along the z-axis (the direction of the shock flow). The grid has $301 \times 301 \times 301$ points, so the structure of the postshock gas (z-direction) is resolved at a scale of 2×10^{14} cm. (At a distance of 440 pc to the Cygnus Loop, this corresponds to 0.″03.)

The lines we are primarily interested in are C IV λ1549 and N V λ1240, both of which are strong resonance lines detected in the STIS spectrum presented by SBRL. We specify the emissivities of these lines and the number density of C^{+3} and N^{+4} based on the fiducial model for the nonradiative shock presented by SBRL. The shock has a velocity of 180 km s^{-1}, and the preshock hydrogen number density is 2 cm^{-3}. The carbon and nitrogen abundances are 8.40 and 7.90 on a logarithmic scale where the hydrogen abundance is 12.00. The shock model is truncated at a swept-up hydrogen column of 10^{17} cm^{-2}. The shock model predictions are combined with the sine wave sheet to produce three-dimensional maps of the line emissivities and number densities of the relevant ionic species. The opacities are derived from average cross sections for thermally broadened profiles. The postshock gas temperature for a 180 km s^{-1} shock is about 4.2×10^5 K, assuming that electrons, protons, and ions are in thermal equilibrium. Using this temperature and oscillator strengths of 0.191 and 0.156 for C IV λ1549 and N V λ1240, respectively (Morton 1991), the cross sections are $\sigma_{\rm C\,IV} R_0 = 32.50$ cm^3 and $\sigma_{\rm N\,V} R_0 = 22.94$ cm^3 (note that $R_0 = 10^{15}$ cm).

The approximation made in the simulations that photons are scattered at a single frequency is valid for moderate line optical depths. For N V and C IV, scattering outside the Doppler core becomes important at optical depths of about 10,000. We now estimate the line optical depths, $\tau_i \sim \sigma_i n_i l$, where σ_i is the cross section (given above), n_i is the ion density, and l is the path length through the emitting region. For the filament viewed edge-on, $l \sim 6 \times 10^{17}$ cm. The shock models predict that the maximum density of C^{+3} and N^{+5} in the postshock flow is 0.0017 and 0.0006 cm^{-3}, respectively. For these maximum densities, $\tau_{\rm C\,IV} \sim 30$ and $\tau_{\rm N\,V} \sim 13$. Note that the typical optical depths through the filament will be smaller than these values, since the average ion densities are much lower. Scattering out of the Doppler core of the lines is not important at these optical depths. Furthermore, the optical depths perpendicular to the sheet are much smaller. We find from the shock model that $N_{\rm C\,IV} = 2.7 \times 10^{12}$ cm^{-2} and $N_{\rm N\,V} = 3.6 \times 10^{12}$ cm^{-2} perpendicular to the shock front. These column densities correspond to optical depths $\lesssim 0.1$ for both lines. Photons can escape quite easily from the sheet in the perpendicular direction, making scattering in the wings even less of an issue. Velocity gradients along the line of sight through the emitting gas can also lead to scattering in frequency. In our

model filament, the shock is moving perpendicular to the line of sight. The velocity spread due to the rippled geometry is of the order of the thermal velocity width—there are no velocity gradients that would make escape of line photons in the wings significant. In summary, we have constructed a model filament where the assumption of scattering at a single wavelength is valid.

The model neglects extinction by dust. To see if this is justified, we estimate the dust opacity along the line of sight through the filament. We assume a standard interstellar medium dust-to-gas ratio in the filament because the nonradiative shock has not yet had time to destroy grains. Equation (7-23) of Spitzer (1978) gives the relationship between the projected area of dust grains per H atom, whence we obtain $\tau_{\rm dust} = 10^{-21} n_{\rm H} l Q_e$. The postshock hydrogen density, $n_{\rm H} \sim 10$ cm^{-3}, is predicted by the shock model. The path length through the filament is $l = 6 \times 10^{17}$ cm, as above. Q_e is the extinction efficiency factor, which is about 2 in the far-ultraviolet (Spitzer 1978, Fig. 7.1). For these values we obtain $\tau_{\rm dust} \sim 0.01$ for a line of sight through the filament. Even if a line photon were to traverse the length of the filament several times, the dust opacity is so low that extinction by grains within the filament could indeed be neglected.

3. RESULTS

In Figure 1 we present model images of the shock as seen in Hα, C IV λ1549, and N V λ1240 emission. Each model has been constructed with 10^7 photons emitted toward the observer (see Appendix in Wood & Reynolds 1999 for details of the photon weighting scheme). The models are calculated for a viewing angle of $\theta = 90°$, $\phi = 20°$ in standard polar coordinates (i.e., tangential to the shock front and 20° from the x-axis). In these images the value at each point is the number of photons detected along that line of sight. The Hα model assumes uniform emission over a very narrow zone (2×10^{14} cm) behind the shock front and, since it is not a resonance line, includes no scattering. The Hα model image (Fig. 1*a*) shows the morphology of the shock front. The C IV λ1549 image shown in Figure 1*b* is what would be observed if there were no scattering. Figure 1*c* is the C IV image with scattering taken into account. Figures 1*d* and 1*e* show the same for N V λ1240. We use the terminology "thin" and "thick" for the two images shown for each line. The thin image is produced by running the code while assuming no scattering. This gives a map of the intrinsic emission from the filament. The thick image includes scattering and is a map of the observed emission. (Note that the term "thick" is used for convenience and is not a statement about the optical depth of the filament. The line optical depth along any given line of sight through the filament can be low even in the thick image.) The results that we present in this section apply only to the model filament described in § 2, and only for the specific input photon number and viewing geometry given above.

Each pair of thin and thick images has been scaled logarithmically between the same minimum and maximum values so they can be visually compared. (All the white spaces outside of the filament have values identically equal to zero.) An inspection of the thick and thin images for each line shows that scattering decreases the intensity significantly along the bright edges of the shock structure. The images also show that the N V emission is more extended than the C IV emission all along the front, as expected from

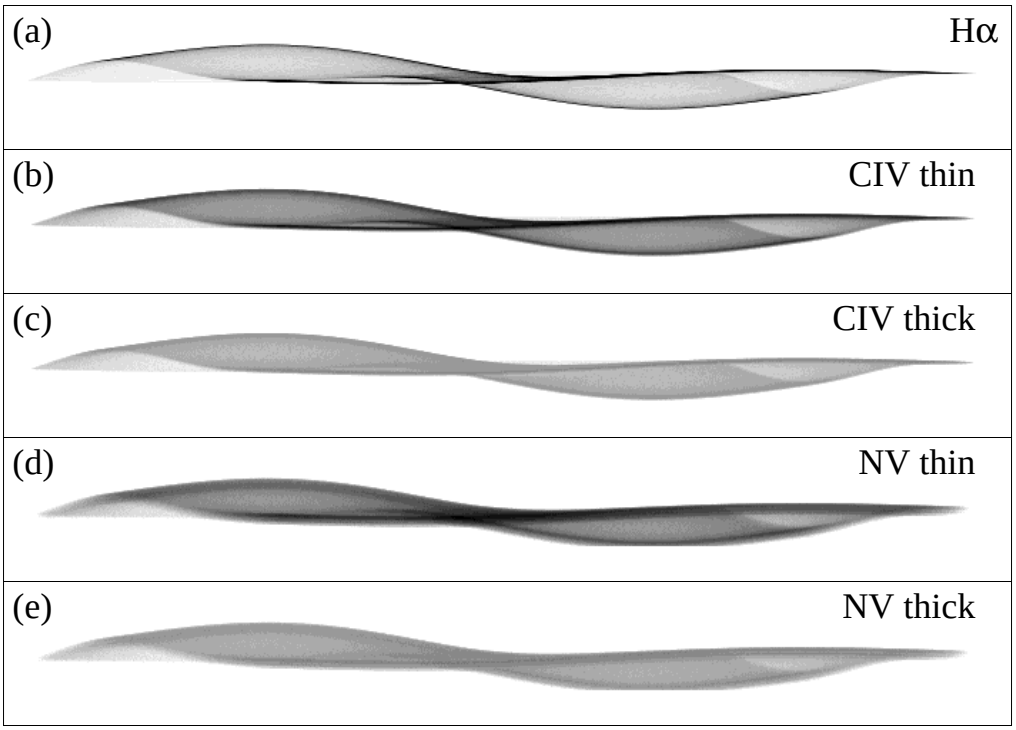

FIG. 1.—Intensity images for the nonradiative shock model: (*a*) optically thin Hα emission, (*b*) optically thin C IV emission, (*c*) optically thick C IV emission, (*d*) optically thin N V emission, and (*e*) optically thick N V emission. Each image corresponds to a spatial extent 7×10^{17} cm by 1×10^{17} cm. The shock moves upward in these figures. The Hα image has been linearly scaled, while each pair of "thin" and "thick" images (i.e., for C IV and N V) has been logarithmically scaled between the same minimum and maximum values for ease of comparison.

shock models (e.g., Fig. 5 of SBRL). Note that because the N v emission is so extended, a small segment (at the trailing edge on the right) has been truncated in the models. Less than 2% of the total photons are lost because of the truncation, and our results are not compromised.

For the selected viewing angle, the model filament is 6×10^{17} cm long (parallel to the shock front) and 5×10^{16} cm wide (crest to trough). The total intensities of the C IV and N v thick images are 4.8×10^6 and 5.6×10^6 photons, respectively. The ratio $I_{\rm thin}/I_{\rm thick}$ is the factor by which the observed intensity of a line has to be multiplied to correct for resonance scattering. $I_{\rm thin}$ is 10^7 for both C IV and N v, so the correction factors for emission from the entire filament are 2.1 and 1.8, respectively. Note that if the sheet were viewed from above (or below) rather than edge-on, then $I_{\rm thick}$ would be greater than $I_{\rm thin}$ for both lines. This is because the scattered flux preferentially escapes in the vertical, optically thin direction.

The C IV and N v emission from the filament has small-scale structure due to the geometry of the shock front and the stratification of the postshock gas. Therefore, we expect the correction factors to depend both on position and on the size of the region included. We first consider regions of the filament that are 5×10^{16} cm along its length and that span its width. The top panel of Figure 2 shows these regions overlaid on the Hα model image. The middle panel

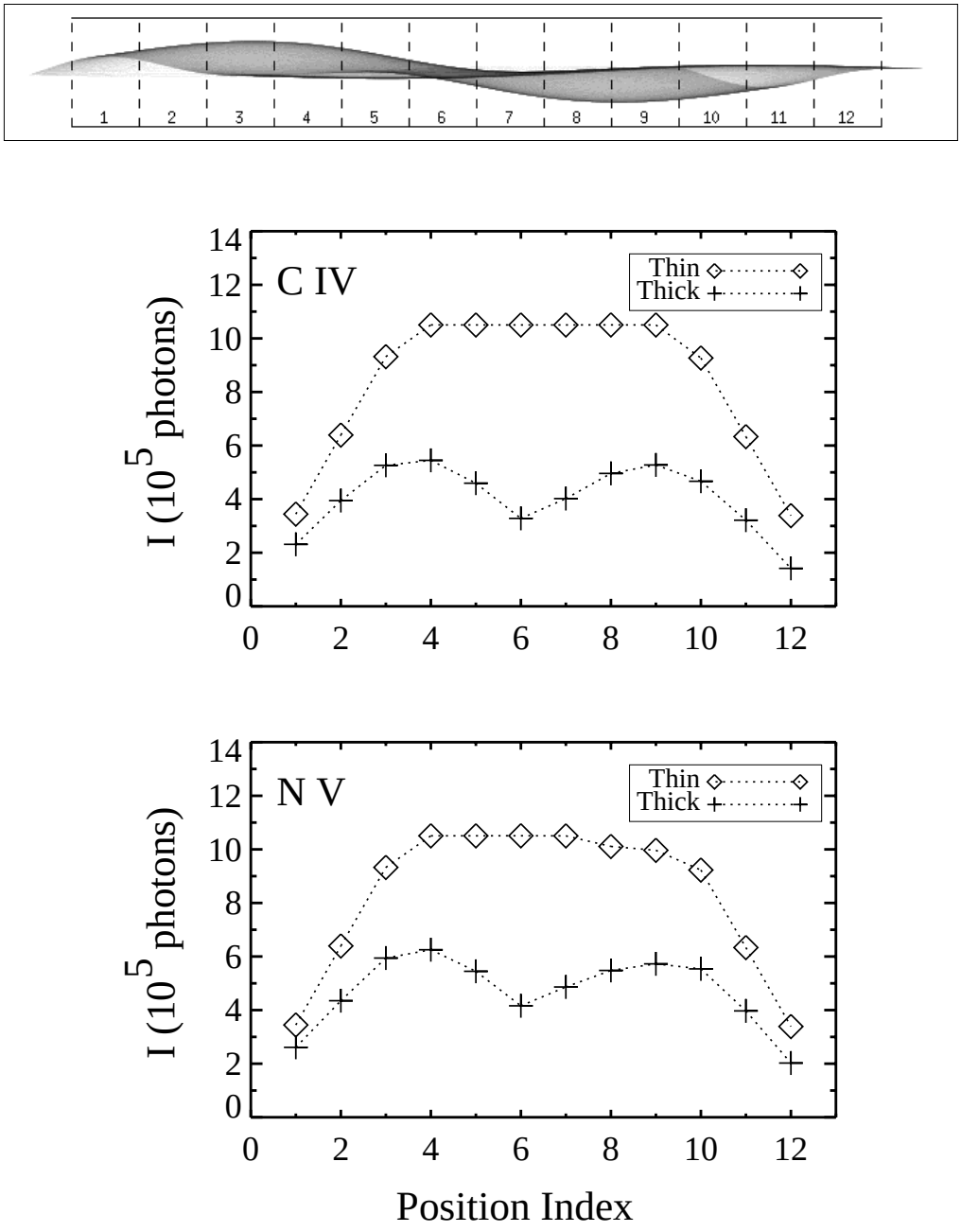

FIG. 2.—*Top*: Hα model image overlaid with a grid. Sections between successive vertical (dashed) lines have been summed to produce the plots in the figure. Each section is 50 pixels wide, corresponding to 5×10^{16} cm. *Middle*: C IV intrinsic (thin) and observed (thick) photon intensities. Each point corresponds to one section of the filament. *Bottom*: N v thin and thick photon intensities. The position index, along the *x*-axis in each plot, is the section number labeled on the Hα model image.

shows plots of the C IV intensities of each region, and the bottom panel shows plots of the N V intensities of each region. The intrinsic (thin) and observed (thick) intensities are shown for both lines. The position index (along the x-axes) corresponds to the region number as labeled in the Hα image. The intrinsic intensity of both lines is fairly constant for regions 3 through 10. In each of these regions, the C IV intensity is about 10.6×10^5 photons, and the N V intensity is about 10.5×10^5 photons. The observed intensities, which take into account resonant scattering, are significantly lower. The C IV correction factor is higher than the N V correction factor for every region. The correction factors in regions 3 through 10 range between 1.8 and 3.2 for C IV and between 1.6 and 2.5 for N V. For both of the lines, resonance scattering has its maximum effect (i.e., the correction factor is highest) in region 6, where the filament is the narrowest.

We now consider narrow regions lying parallel to the shock. In the top panel of Figure 3, the N V thick image is shown overlaid with these regions. Each region is 100 pixels (10^{17} cm) along the length of the filament and 6 pixels (6×10^{15} cm) wide. The regions are numbered, and these numbers are used along the x-axis in the plots. The middle panel shows plots of the C IV intensities of each region, and the bottom panel shows plots of the N V intensities. The intrinsic (thin) and observed (thick) intensities are shown in each case. Of the five selected regions, four are along bright shock tangencies; the exception is region 2, where the emis-

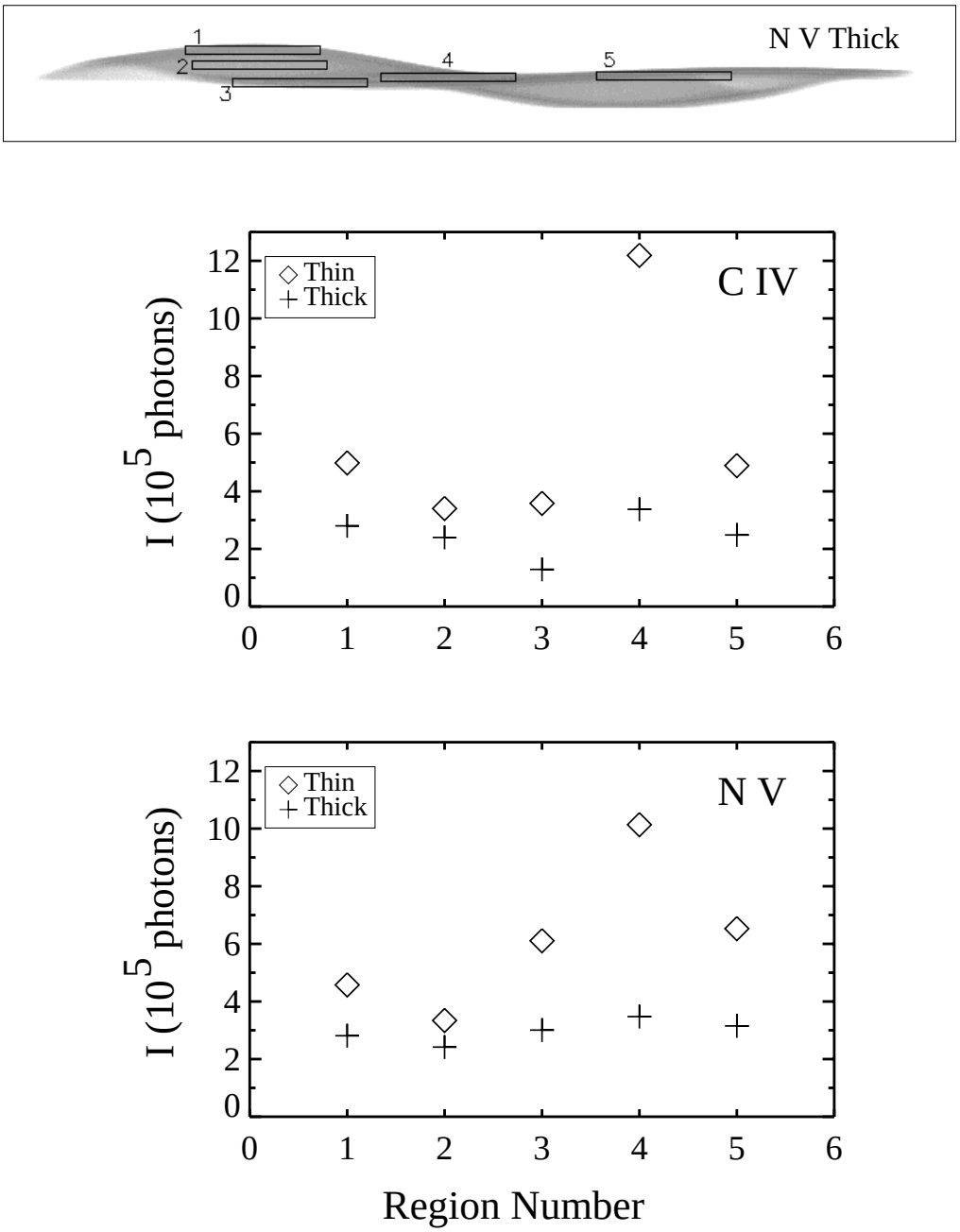

FIG. 3.—*Top*: N V thick model image with several regions overlaid. Each region is 100 pixels long and 6 pixels wide (10^{17} cm by 6×10^{15} cm). *Middle*: C IV intrinsic (thin) and observed (thick) photon intensities for each region. *Bottom*: N V thin and thick photon intensities. The region numbers in each plot are shown along the x-axis and correspond to the numbers marked on the N V image in the top panel.

sion is more diffuse. This region has the lowest correction factors for both C IV and N V. The ratio of $I_{\rm thin}$ to $I_{\rm thick}$ for each line is 1.4 in region 2. Region 4 lies along the narrowest and brightest part of the filament. As expected, the correction factors are highest for this region. The correction factor is 3.6 for C IV and 2.9 for N V. The N V emission from regions 3 and 5 are very similar—3.0×10^5 and 3.1×10^5 observed photons, respectively, with correction factors of 2.0 and 2.1. The C IV emissions from these regions are quite different. There are 1.3×10^5 observed photons from region 3 and 2.5×10^5 observed photons from region 5; the correction factors are 2.8 and 2.0 for regions 3 and 5, respectively.

The intensities and correction factors presented so far are for regions of different sizes, with no regard to spatial variations within a region. We now consider the spatial structure of the emission across the filament. In Figure 4 (*top*), the Hα model is shown, overlaid with three boxes representing spectrograph slits. Each box is 3 pixels (3×10^{15} cm) wide and 45 pixels long. The left panels are plots of C IV intensities and the right panels are plots of N V intensities. Thin and thick intensities have been plotted as functions of position along the slit. The bright tangencies seen in the Hα image have corresponding peaks in the intrinsic (thin) C IV and N V intensities. The leading and trailing edges of the filament structure are clearly seen for all the slits. In addition, for slit *b*, there is a peak at $x \sim 23$. As expected from the shock model used (§ 2; see also Fig. 1), the emission peaks are more pronounced and narrower in C IV than in N V. The effect of resonance scattering is to level these peaks

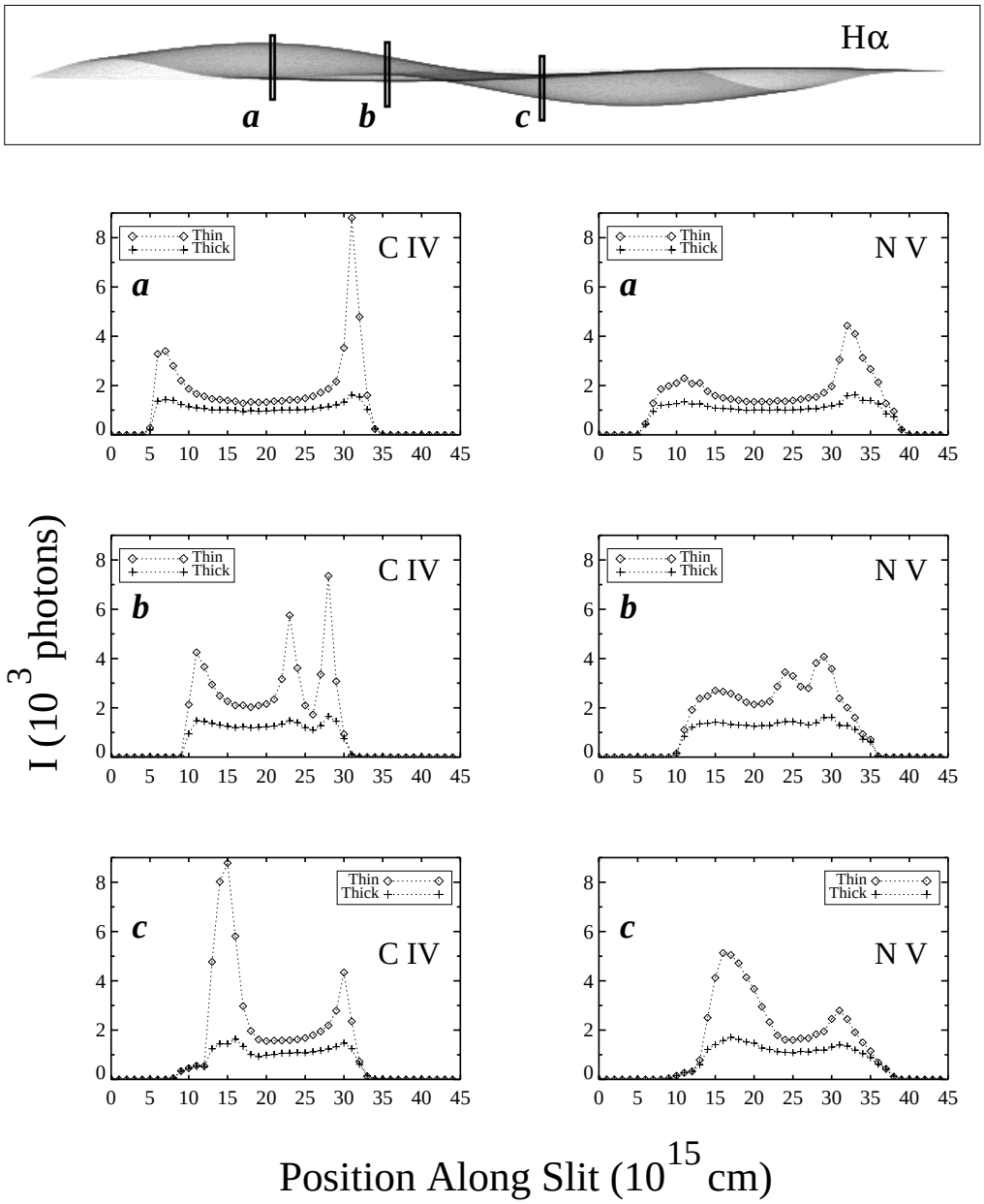

FIG. 4.—*Top*: Hα model image shown overlaid with three boxes representing spectrograph slits. Each box is 3 pixels wide and 45 pixels long. The boxes are labeled *a*, *b*, and *c*. In the plots, the C IV and N V intensities are plotted as a function of position along each of these boxes. Plots along the left column show the C IV thin and thick intensities; plots along the right column show the N V thin and thick intensities. The origin of the *x*-axis corresponds to the top of the slit in each case, so the shock direction is right to left in these plots. The *y*-axis scale is the same for all plots for ease of comparison.

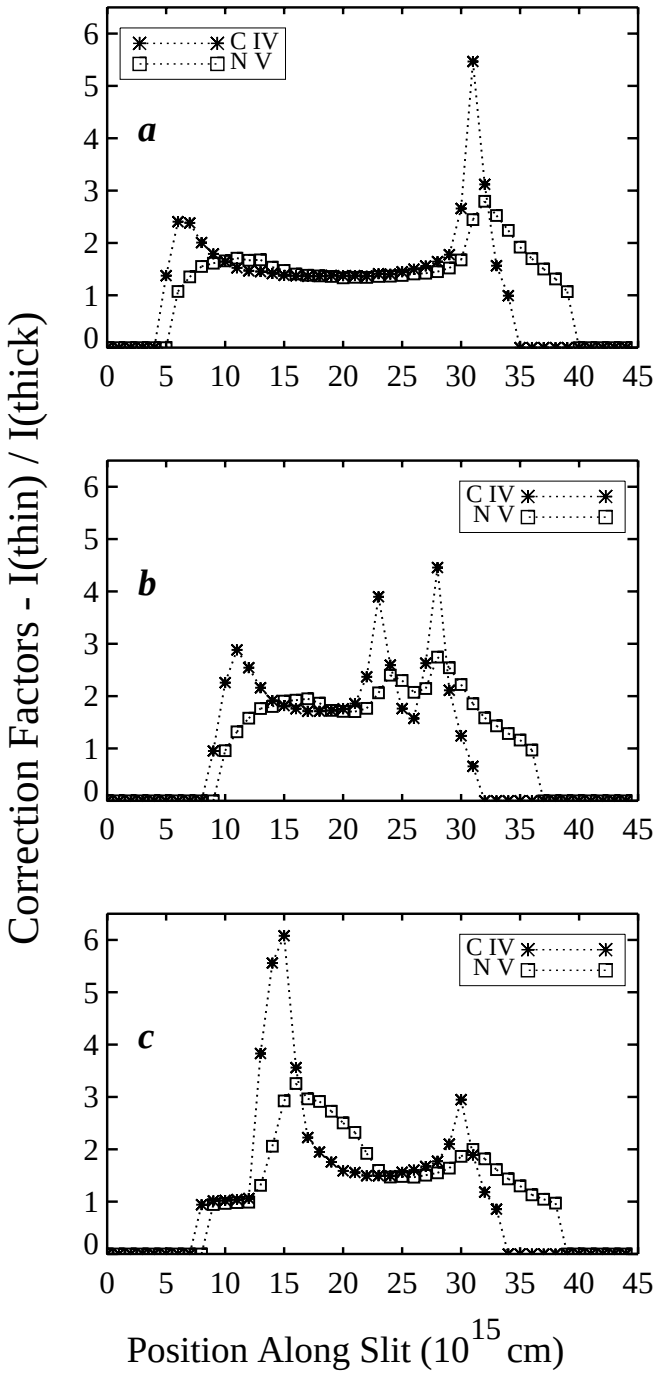

FIG. 5.—Plots of correction factors as functions of position along the slit for the three slit positions shown in Fig. 4.

and produce more uniform emission along the slit. This is evident from the plots in Figure 4. For both lines and all three positions, the variation in the thick intensity across the slit is less than a factor of 2 (excluding the ends, where the intensity is dropping off to zero). In contrast, the maximum thin intensities along the slit are factors of between 3 and 7 higher than the minimum (again excluding the ends).

The correction factors for C IV and N V depend upon location within the slit. They also depend upon the number of spatial points that are binned together. Summing up all the emission in the slit, the correction factors are as follows: (*a*) 1.9 for C IV and 1.7 for N V; (*b*) 2.3 for C IV and 1.9 for N V; and (*c*) 2.4 for C IV and 2.0 for N V. The correction factors do not differ by much among the three slit positions. Also, as in the regions considered earlier, the C IV correction factor is higher than the N V correction factor in each case. In Figure 5, the correction factors are plotted as functions of position along the slit for each of the three slit positions. (Although the information here is available in the plots of Fig. 4, we present it separately for clarity.) The correction factors for C IV and N V are most different from each other at the bright edges of the filament. When the edge is more or less straight, the correction factors are the highest. For instance, at $x \sim 30$ in slit *a* and at $x \sim 15$ in slit *c*, the C IV correction factor is ~ 6, and the N V correction factor is ~ 3. The correction factors are lower, and the contrast between C IV and N V is smaller, on curved edges ($x \sim 7$ in *a*, $x \sim 12$ in *b*, and $x \sim 16$ in *c*).

4. DISCUSSION

The C IV and N V line fluxes are important diagnostics of shock properties. In a nonradiative shock, the postshock gas is in the process of reaching the highest ionization state it can, and so the C IV-to-N V flux ratio is very sensitive to both the shock velocity and the column swept up by the shock. For instance, in the shock model that we have used for this paper ($v_s = 180$ km s^{-1} and $n_0 = 2$ cm^{-3}), the C IV-to-N V flux is 2:1 when the swept-up column is $\sim 8 \times 10^{15}$ cm^{-2}, and is 1:1 when the swept-up column is $\sim 1.6 \times 10^{16}$ cm^{-2}. (The C IV and N V fluxes are also linearly dependent on the carbon and nitrogen abundances, respectively.) The results of the radiative transfer simulation (presented in § 3 above) have shown that resonance scattering decreases the C IV and N V fluxes significantly. The correction factors for these lines, which we have defined as the ratio of intrinsic to observed flux, depend upon the location and the size of the region being observed. These correction factors vary between about 1.5 and 6 for the cases we have considered.

We can apply our current results to the HUT spectrum of the filament presented by Long et al. (1992; this is the same filament on which we have based our model). The spectrum was obtained through an aperture 9.″4 × 116″, which corresponds to a linear size about that of the model filament. Therefore, the correction factors for emission from the entire filament, 2.1 for C IV and 1.8 for N V (§ 3), are applicable to the respective line strengths measured in the HUT spectrum. Since the detailed morphology of the filament was unknown, Long et al. (1992) underestimated the C IV and N V optical depth and did not correct for resonance-line scattering. It is not our purpose here to reanalyze the HUT data. It is, in any case, not possible to do so based on just two correction factors, since there are several resonance lines in the spectrum. Furthermore, most of the results in Long et al. (1992) were based on flux ratios rather than fluxes and would not change drastically. Our aim is to underscore the point that high spatial resolution data have made it worthwhile, and even necessary, to calculate the effect of resonance-line scattering accurately.

Even though we have considered radiative transfer models for only one set of parameters and a single shock geometry, we can infer some general results for nonradiative shocks. For instance, when regions large enough to average over the shock structure are considered, the C IV correction factor is larger than the N V correction factor, but it is less than twice as large. Also, the correction factors for both

lines are highest at places where the filament is narrowest. The contrast between C IV and N V correction factors is maximum at the filament edges. We expect these results to hold for sheetlike shock geometries for a range of shock conditions where the extent of the C IV and N V zones are comparable to those in the models presented here. In order to interpret spatially resolved spectra where different regions of a single filament are sampled, a model using just one set of input parameters is insufficient. Even for a fixed shock geometry (using Hα imaging as in the case of the Cygnus Loop filament, for example), the influence of resonance scattering on line fluxes would depend on the postshock structure, and a grid of models for a range of shock parameters would need to be calculated.

We have been able to specify the geometry of the nonradiative filament in a straightforward way since the shock front is smooth. In contrast, most of the bright optical filaments in SNRs are associated with radiative shocks (e.g., Raymond et al. 1991, Blair et al. 1992) and have complex morphologies. These shocks are subjected to thermal instabilities, and the material in the postshock flow is often knotty and fragmented. The Monte Carlo radiative transfer models can be applied to these shocks only if the density structure of the emitting gas is prescribed. The physically correct way to do this would be to calculate hydrodynamic simulations of the shock interaction. A realistic simulation would need to be done in at least two dimensions to capture the instabilities, and it would have to include cooling, which plays an essential role in the shock dynamics.

We thank the referee for a careful reading of the paper and constructive comments. We also thank John Raymond, with whom we had helpful discussions. This work has been supported by STScI grant GO-07289.01-96A to Johns Hopkins University and by NASA grant NAG 5-6039.

REFERENCES

Blair, W. P., et al. 1991, ApJ, 379, L33
Blair, W. P., Sankrit, R., Raymond, J. C., & Long, K. S. 1999, AJ, 118, 942
Code, A. D., & Whitney, B. A. 1995, ApJ, 441, 400
Cornett, R. H., et al. 1992, ApJ, 395, L9
Hester, J. J. 1987, ApJ, 314, 187
Long, K. S., Blair, W. P., Vancura, O., Bowers, C. W., Davidsen, A. F., & Raymond, J. C. 1992, ApJ, 400, 214
Morton, D. C. 1991, ApJS, 77, 119
Raymond, J. C. 1991, PASP, 103, 781
Raymond, J. C., Black, J. H., Dupree, A. K., Hartmann, L., & Wolff, R. S. 1980, ApJ, 238, 881
———. 1981, ApJ, 246, 100
Raymond, J. C., Blair, W. P., Long, K. S., Vancura, O., Edgar, R. J., Morse, J., Hartigan, P., & Sanders, W. T. 1997, ApJ, 482, 881
Raymond, J. C., Hester, J. J., Cox, D., Blair, W. P., Fesen, R. A., & Gull, T. R. 1988, ApJ, 324, 869
Sankrit, R., Blair, W. P., Raymond, J. C., & Long, K. S. 2000, AJ, 120, 1925 (SBRL)
Spitzer, L. 1978, Physical Processes in the Interstellar Medium (New York: Wiley)
Witt, A. N. 1977, ApJS, 35, 1
Wood, K., & Reynolds, R. J. 1999, ApJ, 525, 799
Yusef-Zadeh, F., Morris, M., & White, R. L. 1984, ApJ, 278, 186